

The swinging counterweight trebuchet

Experiments on inner movement and ranges

Erik Horsdal, Filip Drejer Johnsen and Jonas Rasmussen

Department of Physics and Astronomy, Aarhus University, DK-8000 Aarhus C,
Denmark

E-mail: horsdal@phys.au.dk

Abstract. The inner movement of a trebuchet with swinging counterweight was measured inside a laboratory by the use of rotation sensors to determine angular coordinates for beam, counterweight and sling. Data collection was started before the trebuchet was fired and lasted until some time after the projectile was released and flung into ground right in front of the machine. A single measurement is then sufficient for a semi-empirical determination of longest range and kinetic energy at target as well as mechanical energies and internal forces throughout the entire shot. Loss of mechanical energy was ascertained and attributed to friction. Measurements of actual ranges performed on a flat field with little wind are presented and compared with the semi-empirical determinations and ab initio calculations.

1. Introduction

Trebuchets are historical engines of war. At their peak, they hurled heavy stones at castles under siege from long distances and caused great destruction. Discussions of the use, development, and physics of these artillery pieces can be found in [1, 2, 3, 4, 5, 6]. There is little doubt that the trebuchet became the most important siege weapon during a period of the late Middle Ages before it was overtaken by cannons and gunpowder, but in spite of this, only little information exists on the precise achievements and dimensions of historical trebuchets, and a generally accepted standard for their performance is also lacking [7]. Aside from their continuing historical interest, trebuchets also have enjoyed some attention in practical teaching of classical mechanics [8, 9, 10, 11] because the internal movement touches on many important concepts.

A relatively small experimental trebuchet that could be handled safely by one or two persons inside a laboratory was built and equipped with sensors for the measurement of all angular movements during a shot. The position \mathbf{r} and velocity \mathbf{v} of the projectile at any time prior to its release can be calculated from these data and perceived as initial conditions for a ballistic trajectory from which the range can be extracted as a function of release time or position. We focus on longest range and the energy at target that follows, but internal forces, mechanical energies and their reduction due to internal friction can also be calculated both before and after the projectile is released.

The trebuchet was taken out in the open on warm and calm days for the measurement of actual ranges on a flat field. Two sling lengths and two projectiles in the form of natural, round stones were used. Many shots had to be fired before a maximum range and its random error could be determined. Some were carried out with different settings of the release mechanism, and others as repetitions under identical conditions, as far as possible, to expose random errors.

2. Experimental arrangement and procedures

2.1. The trebuchet and angular measurements

Schematic diagrams of the trebuchet are shown in figure 1. The linear dimensions identified in figure 1a are the long and short segments of the beam L_1 and L_2 , respectively, the length L_3 of the arm that holds the counterweight, and the sling length L_4 . The height of the pivoting axle P for the beam is H , and m and M are the projectile and counterweight masses, respectively. Rotation sensors on the engine

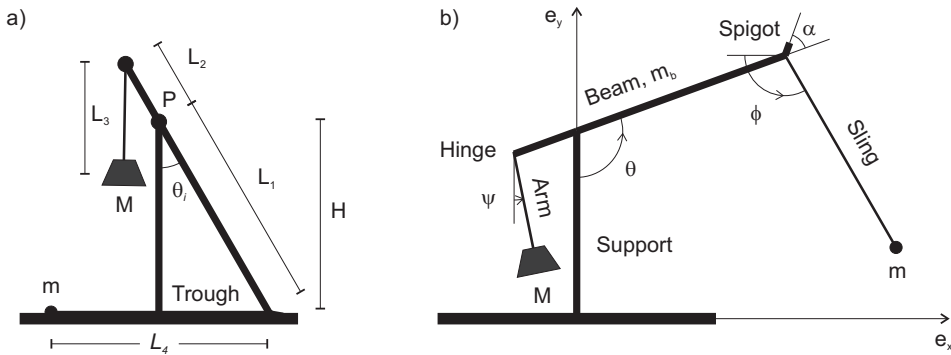


Figure 1. a) Initial configuration, projectile in trough. b) Shortly after lift-off.

measure the respective angular coordinates θ , ψ and ϕ of beam, counterweight, and sling as functions of time. These angles and their orientations are shown in figure 1b. Two are measured from the vertical direction (θ , ψ) and one from the horizontal ϕ .

Photographic images are found in figure 2. The configuration before a shot is

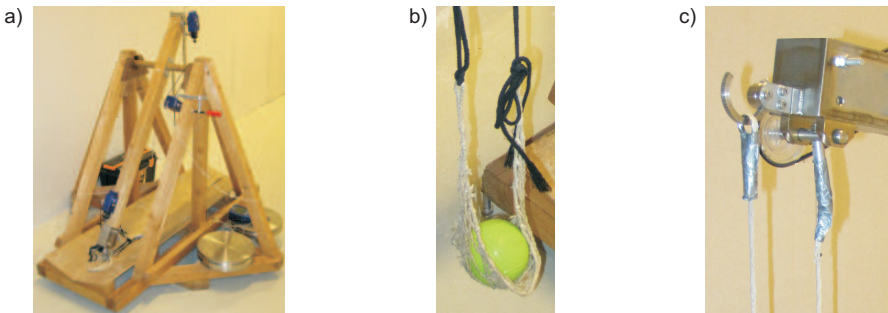


Figure 2. a) Trebuchet with beam in initial position. Three blue rotation sensors. b) Projectile and pouch. c) Two cords of sling. One hanging from semicircle.

displayed in figure 2a, but the sling is empty and the counterweight is not mounted. It consists of a few stainless steel discs, each weighing $\simeq 10\text{kg}$, and two are seen in the foreground on the base next to the trough and trestle. Three blue rotation sensors are also visible. Figure 2b shows the pouch of the sling with a projectile (tennis ball), and in figure 2c one sees the spigot (open end of adjustable semicircle) and the two cords of the sling. One is tied permanently to a pin welded perpendicular onto a stainless steel axle that carries a wheel at the far end for angular measurement. The other is tied to a ring held by the semicircle on which it slides as a shot progresses, and as soon as the direction of the sling becomes perpendicular to the spigot, the ring slides off and the pouch opens. This is the release mechanism for the projectile. Details are given in figure 3a and 3b. The axle is supported by low friction ball bearings, and the

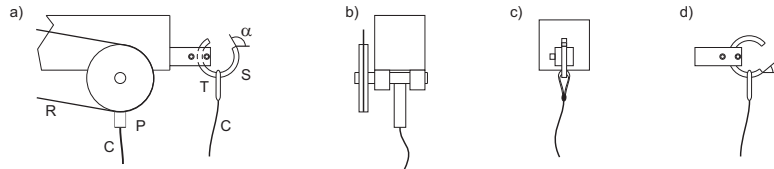


Figure 3. Beam and attachment of sling. a) Side view. Cord C connected to pin P. Second cord C with ring T, semicircular spigot S and angle α . Rubber band R connects to sensor on beam. b) End view without spigot. Pin, axle, two ball bearings, and wheel. c) End view showing spigot. d) Small spigot angle.

wheel is coupled by a rubber band to an identical wheel on a rotation sensor sitting on the beam. The spigot may be fixed in different positions for different spigot angles α . A large is seen in figure 3a and a small in figure 3d. The length of the long beam section $L_1 = 97.5\text{cm}$ is the distance from pivot to midway between axle and ring as in figure 3a, and the sling length $L_4 = 87.0\text{cm}$ is the vertical distance from the lower side of the beam in horizontal position to a heavy projectile that stretches the pouch. The distance from axle to ring varies during a shot but is always close to 7cm. The projectile therefore moves relative to the beam almost on an ellipse with the focal points a distance $d = 7\text{cm}$ apart. The eccentricity e and semi-major axis $a \simeq 2L_4$ are related to d by $d = 2ea$, so $e \simeq 0.04$. This ellipse is almost indistinguishable from a circle of radius L_4 and center at the midway point. This approximation is used hereafter.

The positions of the three rotation sensors and their couplings are shown in figure 4. All sensors are designed to start an angular measurement from zero and to distinguish

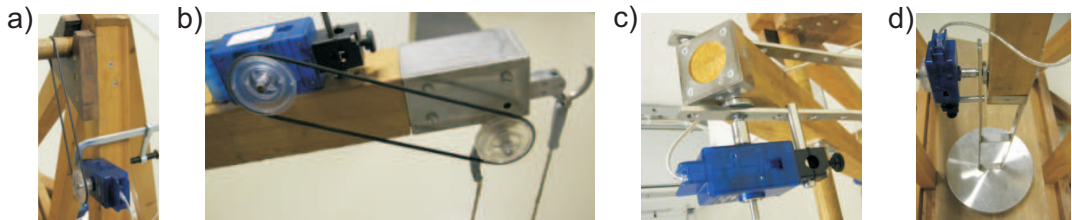


Figure 4. Rotation sensors for: a) Beam θ . b) Sling ϕ . c-d) Counterweight ψ .

between left and right rotations by including a sign which is adjusted subsequently to comply with the conventions in figure 1. The first sensor, seen in figure 4a, is clamped to the trestle and coupled to the pivoting axle of the beam by a rubber band. The experimental beam angle θ_e is thus related to the coordinate angle θ by

$$\theta = k\theta_e + \theta_i, \quad (1)$$

where k is a calibration constant that depends on the diameters of wheel and axle, and θ_i is the initial value of θ . The constant k was determined by varying the orientation of the beam from horizontal to vertical and measuring the resulting variation of θ_e . The correct variation of θ by $\pi/2$ was ensured by the use of sensitive spirit levels. The initial beam angle $\theta_i = 0.55\text{rad}$ was measured by lowering the beam to its initial position from a horizontal orientation ensured again by a sensitive spirit level.

Another sensor, seen fixed to the beam in figure 4b and coupled to the sling as explained above, monitors the angle between beam and sling. The experimental angle ϕ_e measured by the sensor is related to the coordinate angle ϕ for the sling by

$$\phi = \phi_e + k\theta_e.$$

Figures 4c-4d show the third sensor at rest before and after a shot. Its body is fixed to the arm that holds the counterweight and its rotation axle is clamped to a fixed axle that extends from the beam. This sensor monitors the angle between beam and counterweight, and the measured angle ψ_e is related to the coordinate angle ψ by

$$\psi = \psi_e + k\theta_e. \quad (2)$$

2.2. Results of angular measurements

Angles measured as a function of time for beam, counterweight, and sling are shown in figure 5 for three loads: A heavy metallic petanque ball to the left, a light tennis ball

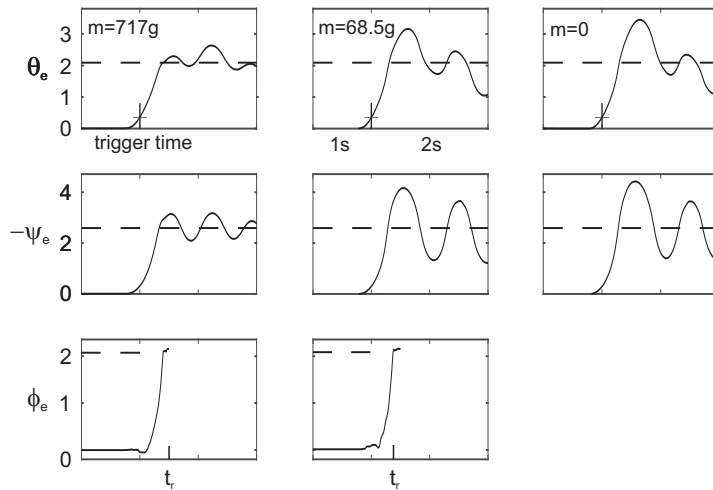


Figure 5. Angular measurements for three loads. Measurements triggered at crosses where $\theta_e = 0.35\text{rad}$. Release time at t_r soon after pin stop at $\phi_e = \pi/2 + \theta_i = 2.12\text{rad}$.

in the middle and a blank shot with no projectile to the right. The sensors were set to sample at a rate of 100Hz and to use a pre-trigger buffer such that data are collected from one second before θ_e passes 20° and to stop two seconds later. The three seconds of acquisition time delivers 300 samples from well before the trebuchet is fired and until well after the projectile has left the pouch. All angles start at zero and broken lines show final values at rest for beam and counterweight. Oscillatory motion is seen in each case. It is strongest in the blank shot to the right, a little damped by the light projectile, and quite significantly suppressed by the heavy, which carries a large fraction of the available mechanical energy after release. The oscillations with smaller amplitude have larger frequency as expected for pendulum motion.

The two measured sling angles in the lowest row of figure 5 are meaningful only from some time after a shot is initiated and until the pin P in figure 3a becomes parallel to the beam and can move no further. The beam was held at rest prior to each shot by a firm grip of the projectile by the operator. The static tension in the cords of the sling therefore drops suddenly as soon as the projectile is set free, and the pin then falls a little to give a false indication of sling direction. However, the tensions soon reach values well beyond the gravity mg of the projectile and this makes the measurements credible, but the motion of the pin is stopped before the projectile is released. This is seen clearly in the data when the sharp increase of ϕ_e is suddenly interrupted.

2.3. Initial motion and moment of inertia for beam

The initial motion of the beam before triggering is shown in figure 6 for the loads

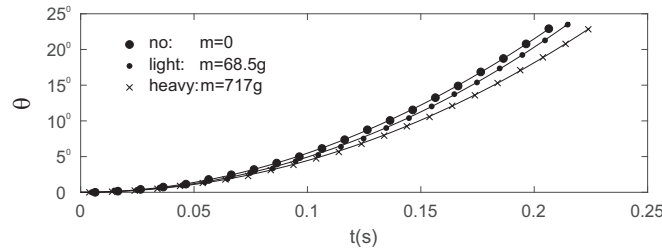


Figure 6. Initial variation of θ vs adjusted time. Full curves, fits determining $\ddot{\theta}_i$.

in figure 5. The start of each shot at $t = t_i$ was found by fitting the function

$$f(t) = \frac{1}{2}\ddot{\theta}_i(t - t_i)^2 + c(t - t_i)^3 \quad (3)$$

to the measured angles after calibration and exclusion of the initial zeros. Newtonian dot-notation is used here and henceforth for time differentiation. The fitting parameters in (3) are, besides t_i , the initial angular acceleration $\ddot{\theta}_i$ and c .

After replacement of $t - t_i$ by t , equation (3) reads

$$\theta = \frac{1}{2}\ddot{\theta}_i t^2 + ct^3 \quad \text{and} \quad ct \ll \ddot{\theta}_i \quad \text{at} \quad t = 0.2s.$$

This is the function shown in figure 6. It fits the data very well so the parameters t_i and $\ddot{\theta}_i$ are determined with good precision. The light projectile damps the acceleration

a little relative to a blank shot, and the heavy projectile lowers it significantly. We find $\ddot{\theta}_i = 19.2\text{rad/s}^2$ and 16.0rad/s^2 for the blank shot and the heavy projectile, respectively. The initial acceleration of the projectile is $L_1 \cos \theta_i \ddot{\theta}_i$, which is somewhat larger than the gravitational acceleration g in both cases.

Similar measurements and analysis with the beam alone, starting from a horizontal position ensured by a sensitive spirit level, gives $\ddot{\theta}_{ih} = (-12 \pm 1)\text{rad/s}^2$, and this quantity is related to the moment of inertia \mathcal{I}_b for the beam relative to the pivoting axle by

$$\mathcal{I}_b \ddot{\theta}_{ih} = -m_b g L_{CM}, \quad \text{Newton's second law for rotation,}$$

where m_b is the beam mass and L_{CM} the pivot to center of mass distance. These two parameters were determined by weighing and balancing the beam with all its attachments. This leads to $\mathcal{I}_b = 1.85 \pm 0.15\text{kgm}^2$.

Table 1 collects all parameters of the trebuchet, and includes also the calculated

| L_1 cm | L_2 cm | L_3 cm | L_4 cm | M kg | L_{CM} cm | m_b kg | \mathcal{I}_b kgm^2 | θ_i rad | H cm | ΔU J |
|-------------|-------------|-------------|-------------|-----------|----------------|-------------|-----------------------------------|-------------------|-----------|-----------------|
| 97.5 | 25.0 | 51.5 | 87.0 | 53.9 | 46.5 | 4.86 | 1.85 ± 0.15 | 0.55 | 83.1 | 204 |

Table 1. Parameters of trebuchet. M includes 5 discs and their movable support.

height of the fulcrum $H = L_1 \cos \theta_i$ and the potential energy invested when the engine is loaded

$$\Delta U = (ML_2 - m_b L_{CM})g(1 + \cos \theta_i). \quad (4)$$

Among these parameters, the moment of inertia \mathcal{I}_b is considered the most uncertain. The semi-empirical ranges and energies at target extracted from the angular measurements do not depend on the value of \mathcal{I}_b in table 1, but it is important for the determination of dynamic variables like the mechanical energy of the engine and internal force. The measured value of \mathcal{I}_b was therefore investigated further, see Appendix A.

2.4. Motion of counterweight

The position of the counterweight is

$$\mathbf{r}_M = H \mathbf{e}_y - L_2(\sin \theta \mathbf{e}_x - \cos \theta \mathbf{e}_y) + L_3(\sin \psi \mathbf{e}_x - \cos \psi \mathbf{e}_y),$$

where θ and ψ are related to the measured angles θ_e and ψ_e by (1) and (2), and \mathbf{e}_x and \mathbf{e}_y are unit vectors shown in figure 1b. Apart from the two measured angles, the position \mathbf{r}_M depends only on the height of the fulcrum H and the lengths of the short beam section L_2 and the arm for the counterweight L_3 .

The path of the counterweight is illustrated in figure 7 for the two projectile masses in figure 5. Figure 7a and 7b show that the counterweight falls steeply from the initial position at M until the fall is suddenly stopped and an oscillatory motion back and forth begins. In figure 7a, the trajectory of this final motion lies quite close to a circle of radius $L_2 + L_3$ centered at the pivot P and the circle is touched every time the configuration of counterweight and beam is stretched out. This motion is much

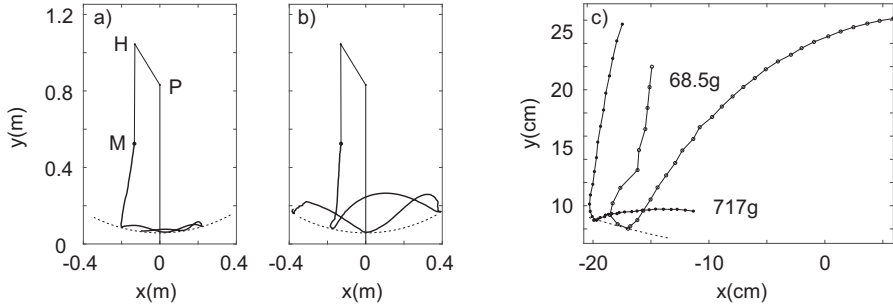


Figure 7. Motion of counterweight. a) $m = 717\text{g}$. b) $m = 68.5\text{g}$. c) Details.

less violent than the motion shown in figure 7b with the lighter projectile where large excursions are seen both sideways and up down.

The transition from fall to oscillations is shown in more detail in figure 7c. Neighboring points are separated in time by 10ms so the density of points reflects speed. This is seen to be reduced rather significantly at the transition with the heavy projectile, but it is almost constant with the light one, and for this it is even possible, with good will, to see a resemblance to elastic reflection off the circle including equal angles of incidence and reflection. This is the theoretical behavior expected for an infinitely heavy counterweight: Like a ball that falls from rest over a hemispherical bowl and bounces back elastically, the counterweight first drops vertically and thereafter goes into a series of free falls interrupted by elastic reflections.

2.5. Motion of projectile and estimates of ranges, efficiencies and merits

The position of the projectile has the same form as the position of the counterweight

$$\mathbf{r}_m = H\mathbf{e}_y + L_1(\sin \theta \mathbf{e}_x - \cos \theta \mathbf{e}_y) - L_4(\cos \phi \mathbf{e}_x + \sin \phi \mathbf{e}_y). \quad (5)$$

The functions \mathbf{r}_m and $\mathbf{v}_m = \dot{\mathbf{r}}_m$ may be taken as initial conditions for ballistic trajectories in vacuum. A range function, that depends on time or position of release, can be extracted from these, see Appendix B.1. For the light projectile in figure 5 and other parameters as in table 1, we find the results shown in figure 8. The projectile's trajectory near the position for longest range is plotted in figure 8a, and the configuration of beam and sling at this position is shown. Note that the path is not perpendicular to the sling

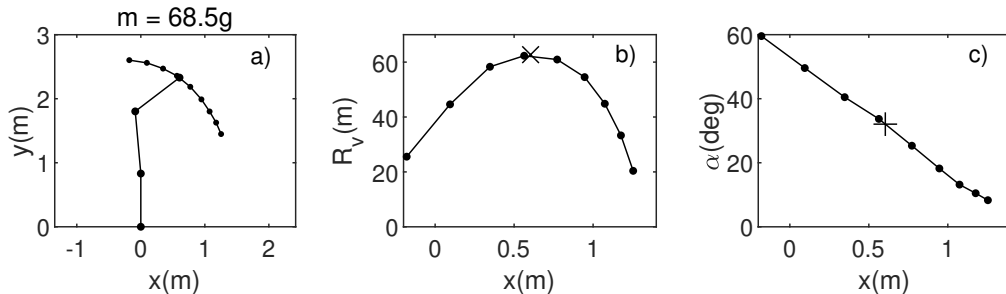


Figure 8. a) Path of light projectile in sling. b) Range in vacuum. c) Spigot angle.

because the spigot moves to the left. Figure 8b shows calculated vacuum ranges R_v plotted as a function of horizontal release position. There is a clear maximum of $\simeq 62\text{m}$ near $x = 0.6\text{m}$. Spigot angles α are shown in figure 8c where it is seen that a setting close to 32° leads to maximum range.

Similar results for the heavy projectile in figure 5 is shown in figure 9. The maximum range in vacuum is reduced to $\simeq 36\text{m}$ and is found near $x = 0.75\text{m}$ for $\alpha \simeq 50^\circ$. Note that $\theta < \pi$ at the critical configuration while $\theta > \pi$ in figure 8a.

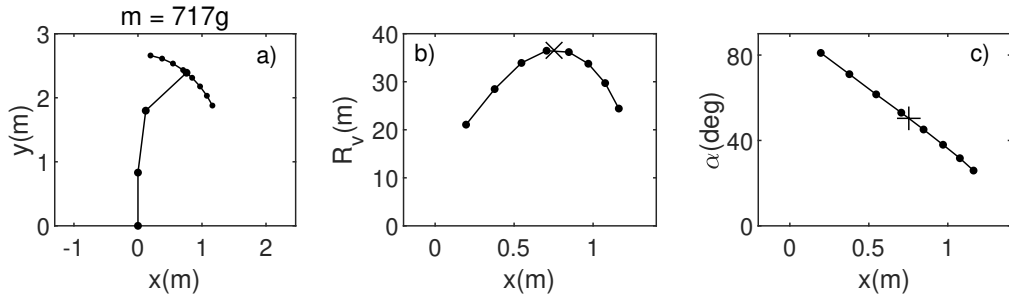


Figure 9. a) Path of heavy projectile in sling. b) Range in vacuum. c) Spigot angle.

Numerical results for the longest vacuum ranges in the two cases are collected in table 2. The ranges are given first next to the projectile masses, and then the best release times t_r and spigot angles α . The initial values for the ballistic paths are positions (x_i, y_i) , speeds v_i and climbs A . The ends of the trajectories are at $(-R_v, 0)$ where the speed in vacuum is v_f and the kinetic energy $T_v = \frac{1}{2}mv_f^2$. The values of T_v should be compared to the invested energy $\Delta U = 204\text{J}$. The light projectile is seen to carry only 11% of ΔU while almost 70% goes to the heavy. The higher efficiency ϵ for the heavy projectile was noted already in the discussion of the results in figure 5 and 7.

| m | R_v | t_r | α | x_i | y_i | v_i | A | v_f | T_v | ϵ | \mathcal{M} | \mathcal{M}_ϵ |
|------|-------|-------|--------------|-------|-------|-------|--------------|-------|-------|------------|---------------|------------------------|
| g | m | s | | m | m | m/s | | m/s | J | % | m·kJ | m·kJ |
| 68.5 | 62.4 | 0.533 | 32.2° | 0.60 | 2.33 | 25.1 | 34.4° | 26.0 | 23.2 | 11 | 1.45 | 0.16 |
| 717 | 36.6 | 0.593 | 50.0° | 0.76 | 2.39 | 18.6 | 39.5° | 19.9 | 141 | 69 | 5.18 | 3.57 |

Table 2. Parameters for longest vacuum ranges R_v with two projectile masses m . Speed v_f and kinetic energy T_v at target. Efficiency ϵ . Merits \mathcal{M} and \mathcal{M}_ϵ .

Special emphasis has been placed on maximum vacuum range, but other parameters could be considered. If both range and damage at target are essential, then the parameter $\mathcal{M} = R_v T_v$ is a more appropriate variable, and the efficiency could also be brought into play as in $\mathcal{M}_\epsilon = \epsilon R_v T_v$, although $\epsilon \propto T_v$ with fixed dimensions as here. We shall refer to such functions as merits of the trebuchet. According to table 2, the heavy projectile outperforms the light by both standards in spite of the shorter range. The given merits are evaluated at the release point for maximum range, and this probably does not result in the largest possible values. We return to the question of optimization in section 3.1.

3. Results and discussion

3.1. Varying projectile mass

Standard tennis and petanque balls supplemented by natural stones with almost spherical shapes and different masses were used as projectiles in a series of measurements with the constant parameters listed in table 1. Maximum vacuum ranges R_v and required spigot angles α were derived for each projectile as discussed in section 2.5, and the results are plotted in figure 10. They show a quite significant decrease of R_v

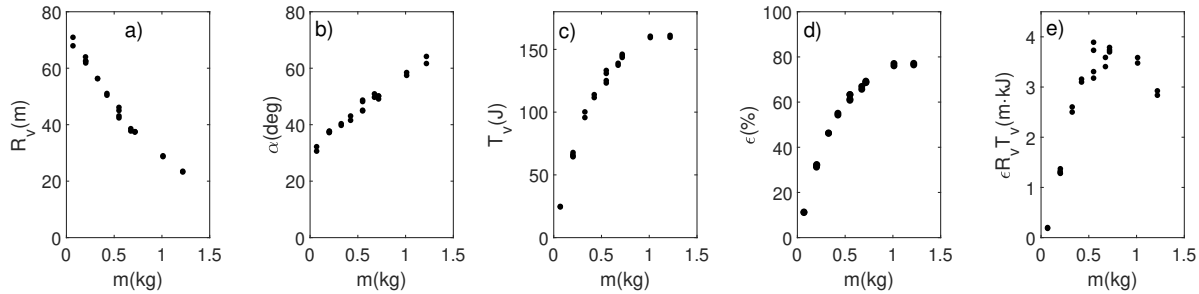


Figure 10. As functions of projectile mass m : a) Maximum vacuum range, R_v . b) Spigot angle, α in degrees. c) Energy at target, T_v . d) Efficiency, ϵ . e) Merit function, $\mathcal{M}_\epsilon = \epsilon R_v T_v$. Repetitions at each m expose statistical errors.

as a function of m and a spigot angle α that increases such that the heavier projectiles swing further relative to the beam than the lighter. The kinetic energy at target T_v was also derived and it shows a strong increase that seems to level off or reach a maximum. The efficiency is likewise seen to be an increasing function of m , and this is taken into account in the merit function $\mathcal{M}_\epsilon = \epsilon R_v T_v$, introduced in section 2.5. \mathcal{M}_ϵ shows a clear maximum close to $m = 0.7\text{kg}$, which is not far from the heavy mass in table 2.

The initial conditions for the longest ballistic trajectories are shown in figure 11. The variable x in figure 11a is the horizontal position of the projectile at release. The

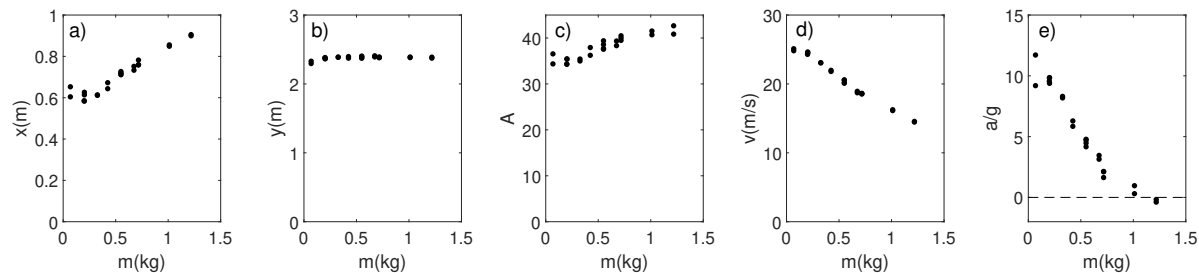


Figure 11. Initial conditions for maximum vacuum range *vs* projectile mass. a+b) Position of projectile at release (x, y). c) Initial climb A in degrees. d) Speed at release v . e) Acceleration along path at release $a = v$ in units of gravity g .

target is found at a negative value of x , so a positive release position subtracts from the range. The variable y in figure 11b is the height at start measured from the base of the trestle, and it is added almost unchanged to the range for a target at ground level. The

initial climb of the projectile A in figure 11c is a little below 45° but approaches this value at large m . The speed at release $v = |\mathbf{v}|$, which is the initial speed in the ballistic projectile path, is shown in figure 11d. It decreases with m and reflects the same trend for the range R_v . The acceleration \mathbf{a} projected on the velocity at release $a = \mathbf{a} \cdot \mathbf{v}/v$ is shown in figure 11e. It is quite large and positive for light projectiles so these are still gaining speed at release for longest range. The range maximizes at an initial climb A of 45° for constant speed, but since speed is increasing for decreasing A , a smaller A is advantageous and figure 11c shows that $A \simeq 35^\circ$ is best for the lightest projectiles.

The merit values \mathcal{M} in table 2 are not maximized, so another release time may increase their values, and this is indeed the case for light projectiles. If release takes place a little later Δt than specified in table 2, the range decreases slowly like $1 - (\Delta t/t_R)^2$, but the energy increases linearly like $1 + \Delta t/t_E$ such that the product increases. Here, t_R depends on the curvature d^2R/dx^2 at maximum and the speed $v_x = v \cos(A)$, and t_E on the acceleration a . The curvature can be read from figure 8 and v , A and a from figure 11. We thus find $t_R \simeq 45\text{ms}$ and $t_R \simeq 110\text{ms}$, which leads to a maximum of \mathcal{M} at $\Delta t \simeq 10\text{ms}$ (the time between measuring points). Here \mathcal{M} has increased by $\simeq 4\%$, the range R is reduced by $\simeq 4\%$ and the kinetic energy T is larger by $\simeq 9\%$. This also improves the efficiency by $\simeq 9\%$ from $\simeq 11\%$ to $\simeq 12\%$. For the heavy projectiles with $a/g \simeq 0$, range and speed maximize almost at the same time, so \mathcal{M} is already at maximum. Optimization is discussed in detail in [7].

Figure 12 shows the configuration of the trebuchet at release expressed by the angular coordinates for beam, counterweight and sling. The beam is close to vertical at $\theta = \pi$ for all projectiles, figure 12a, but while it has just passed this point for the lightest it has not come so far for the heaviest. This was illustrated already in figure 8 and 9. The counterweight angle ψ is small and negative at release, figure 12b, but during

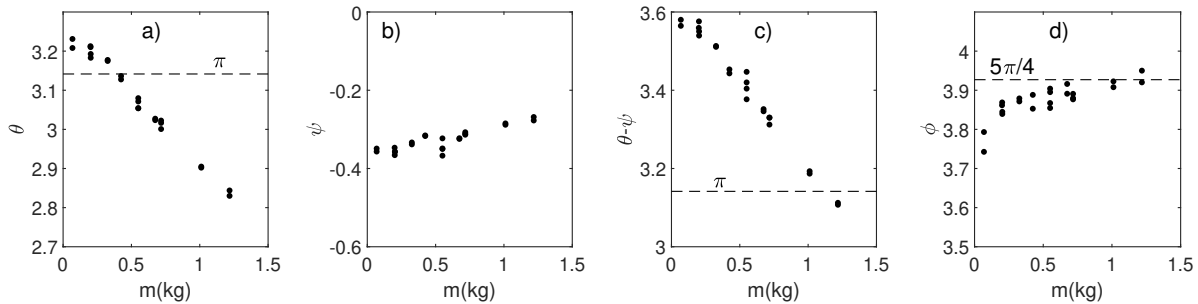


Figure 12. Angular coordinates at release for maximum vacuum range *vs* projectile mass m . Same angular ranges of 0.6 radians. a) Beam, θ . b) Counterweight, ψ . c) Beam and counterweight, $\theta - \psi$. d) Sling, ϕ .

a shot it starts from zero and is first positive before it becomes negative. The angle between beam and counterweight, $\theta - \psi$, is shown in figure 12c. The configuration is stretched out when $\theta - \psi = \pi$, and this happens near $m = 1\text{kg}$ or close to maximum merit and an initial climb of $A = 45^\circ$. The sling angle ϕ shown in figure 12d is near $5\pi/4$ at release, or $\pi/4 = 45^\circ$ over the horizon as seen also in figure 8 and 9.

3.2. Varying counterweight

Two smaller masses of the counterweight and three projectile masses were used in a series of experiments to illustrate the dependence on counterweight mass M . The other parameters of the trebuchet are listed in table 1. Figure 13 shows the longest vacuum

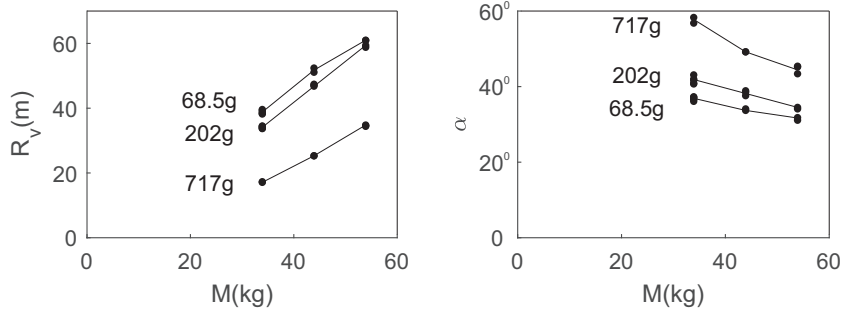


Figure 13. Maximum vacuum ranges R_v and spigot angles α vs counterweight M . Projectile masses next to curves.

range R_v and the required spigot angles α . A lighter counterweight clearly leads to a significant reduction of range irrespective of projectile mass.

3.3. Varying sling length

Maximum vacuum ranges R_v and corresponding spigot angles α were determined also for a number of sling lengths L_4 and two projectile masses m . Other parameters of the trebuchet are listed in table 1. The ranges R_v for the two masses are shown in figure 14 and each shows a broad maximum located close to the sling length L_4 of 0.87m used in

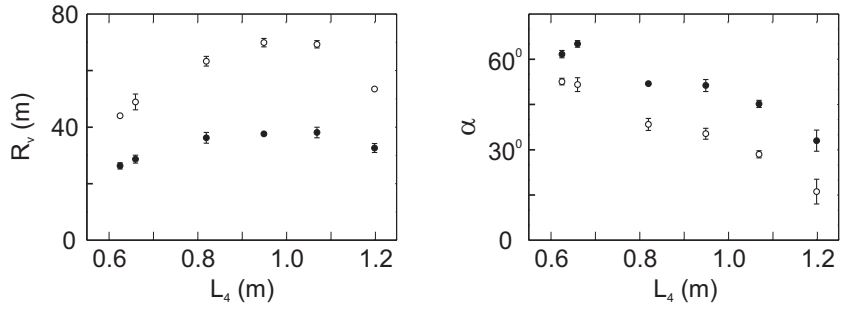


Figure 14. Maximum vacuum ranges R_v and spigot angles α vs sling lengths L_4 . Open points: $m = 170$ g. Full points: $m = 700$ g.

the previous measurements. The spigot angle α varies significantly with L_4 such that a longer L_4 implies a smaller α and vice versa.

3.4. Mechanical energy

The potential energy of the trebuchet is assumed to be zero when the counterweight is at rest in its lowest position and a projectile lies ready in the trough at ground level.

The initial mechanical energy prior to a shot is then the potential energy ΔU in (4) added during loading, and the mechanical energy is thereafter either constant or strictly decreasing because of irreversible losses.

The mechanical energy is the sum of all kinetic and potential energies. For the degrees of freedom in figure 1, the total kinetic energy is

$$T = \frac{1}{2}m\dot{\mathbf{r}}_m^2 + \frac{1}{2}\mathcal{I}_m^{cm}\dot{\phi}^2 + \frac{1}{2}M\dot{\mathbf{r}}_M^2 + \frac{1}{2}\mathcal{I}_M^{cm}\dot{\psi}^2 + \frac{1}{2}\mathcal{I}_b\dot{\theta}^2. \quad (6)$$

The first two terms of the sum is the mechanical energy of the projectile. It has translational and rotational speeds $|\dot{\mathbf{r}}_m|$ and $\dot{\phi}$, respectively, and \mathcal{I}_m^{cm} is the moment of inertia with respect to the center of mass. The next two terms constitute the mechanical energy of the counterweight, and the last term is the mechanical energy of the beam whose moment of inertia relative to the pivoting axle is \mathcal{I}_b . The two terms that represent the energies of rotation for projectile and counterweight contribute only little.

The potential energy for the same degrees of freedom is

$$U = mgy_m + Mg(y_M - y_M^f) + m_bg(y_{m_b} - y_{m_b}^f). \quad (7)$$

Here y_m , y_M and y_{m_b} are the instantaneous heights above ground of the centers of mass for projectile, counterweight, and beam, respectively. The final values at rest after a shot are $y_m^f = 0$, $y_M^f = H - (L_2 + L_3)$ and $y_{m_b}^f = H + L_{CM}$.

The motion of sling (and projectile) is measured until the time when the pin P in figure 3a is stopped by the beam, but the projectile remains in the pouch a little longer. The motion of sling and projectile was calculated in this short interval of time by treating the system as a pendulum in an accelerated coordinate system that follows the spigot. The initial conditions for the motion was determined by the sling motion leading up to the pin stop, and it was followed until the direction of the projectile velocity dips below -45° relative to the horizon, such that a point just in front of the engine is hit. The extrapolation of the motion is short, but important, because mechanical energy is exchanged also here, and it allows all kinetic and potential energies in (6) or (7) to be calculated at all times.

The total mechanical energies of engine (counterweight and beam) and projectile

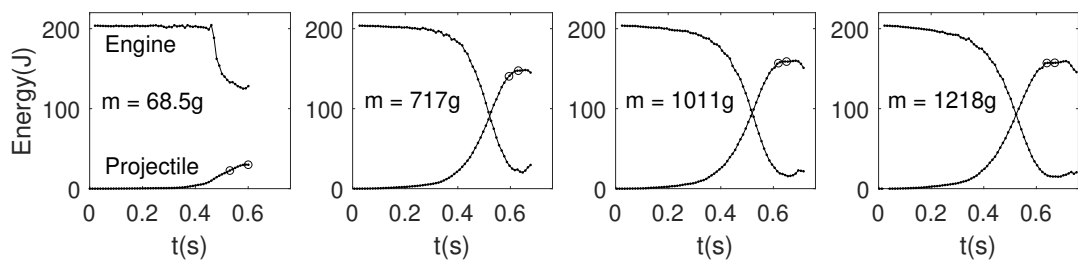


Figure 15. Mechanical energies *vs.* time until release for four projectile masses m .

heaviest projectiles used in the experiments. The release time for longest range followed by the time when the pin is stopped are marked by circles. The energy of the engine

is $\Delta U = 204\text{J}$ at start and a small fraction of this is subsequently transferred to the light projectile whereas the heavier absorb much more. The process is also slower for the heavy projectiles, and the extrapolations from pin stop to actual release are longer. When the projectile leaves the trebuchet, it carries the mechanical energy plotted at the end of the time series. We do not treat this as a lost energy, but include it as a constant contribution to the total energy after release.

Figure 16 shows mechanical energies over the full duration of a measurement with the constant projectile contribution after release represented by horizontal lines. The total energy shows increases over short intervals of time at each projectile mass but most clearly for the lightest. These increases are reproducible and reveal systematic

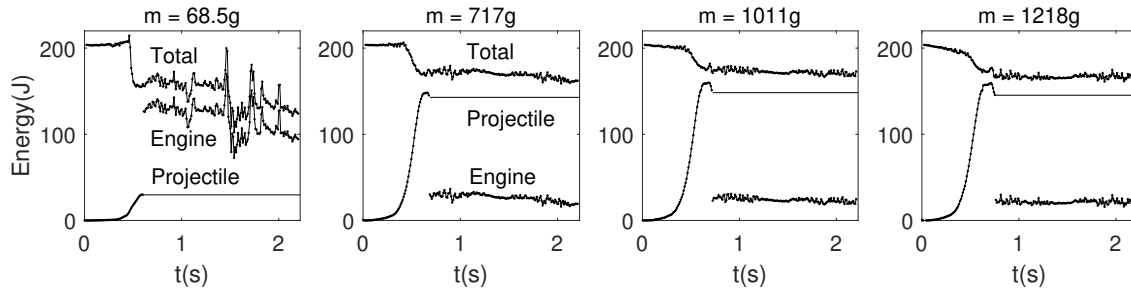


Figure 16. Mechanical energies covering full durations of measurements.

errors. Most are seen after the projectile is released which incriminates the movement of beam or counterweight. The errors are largest with the light projectile for which the inner movement of the engine is quite violent, and even more so for blank shots where the trestle clearly tilts and moves unless extra weight is added, most often by a person standing on the base. The data for the heavier projectiles are less suspicious, but still show increases. We therefore look apart from the long term data for the light projectile, and suspect that one or more degrees of freedom, that absorb and release mechanical energy, are missing in (6) and (7). This could be elastic bending of the beam or a small, undetected movement of the fulcrum due to a flexible trestle. The last possibility was examined by a simple model in which the bearings for the pivoting axle are fixed to a heavy mass that is free to slide without friction on a horizontal surface. When the heavy mass is adjusted to limit the movement to a fraction of a centimeter, we see a few joules of energy being exchanged after about one second so this could be an explanation, but we can not go any further without actual knowledge of the motion, which we do not have. The model also indicates very little influence on range or energy at target, even for strong movement of the bearings. This is because strong horizontal forces are seen only long after the projectile is launched and the counterweight has begun its final, oscillatory motion.

In addition to systematic errors, the data in figure 15 and 16 also suffer from random errors that look like noise. This can be traced to the counterweight's kinetic energy, which depends sensitively on $\dot{\psi}$ and $\dot{\theta}$, but the noise is clearly generated mostly by fluctuations of $\dot{\psi}$. The angle θ therefore seems to be measured more precisely than ψ .

3.5. Loss of mechanical energy to friction and air resistance

Mechanical energy is inevitably lost to friction and air resistance. Friction is found at the bearings for the pivoting axle of the beam where wood moves against wood, and at the hinge for the counterweight where the materials are stainless steel. Air resistance primarily affects the sling motion because of the relatively large aerodynamic cross section of the pouch and the high speed shortly before release of the projectile. The steep fall of total mechanical energy seen near 0.5s in figure 16 is thus tentatively attributed to heat generation when the initial fall of the counterweight is suddenly interrupted, but also to turbulence from fast sling motion although this is less important as will be seen. The magnitudes of the reaction forces at the pivot for the beam $|\mathbf{F}_P|$ and the hinge for the counterweight $|\mathbf{F}_H|$ are then large and so are the respective sliding speeds $R_P\dot{\theta}$ and $R_H(\dot{\theta} - \dot{\psi})$, where R_P and R_H are radii. These factors determine the rate of heat generation as estimated by the standard model for friction

$$P_f = \mu_p |\mathbf{F}_P| R_P |\dot{\theta}| + \mu_H |\mathbf{F}_H| R_H |\dot{\theta} - \dot{\psi}|, \quad (8)$$

where μ_p and μ_H are empirical friction coefficients. The reaction force \mathbf{F}_P balances all other forces that act on the bearings for the beam treated as a rigid body. These are the forces at the hinge \mathbf{F}_H , the center of mass for the beam \mathbf{F}_{CM} , and the spigot \mathbf{F}_S , so we have

$$\begin{aligned} \mathbf{F}_P &= \mathbf{F}_H + \mathbf{F}_{CM} + \mathbf{F}_S \\ &= M(\ddot{\mathbf{r}}_M + g\mathbf{e}_y) + m_b(\ddot{\mathbf{r}}_{CM} + g\mathbf{e}_y) + m(\ddot{\mathbf{r}}_m + g\mathbf{e}_y). \end{aligned}$$

The force $|\mathbf{F}_H|$ is always much larger than $|\mathbf{F}_{CM}|$ or $|\mathbf{F}_S|$, so $|\mathbf{F}_P| \simeq |\mathbf{F}_H|$ throughout a shot. $|\mathbf{F}_P|$ is shown in figure 17 after division by g to make the force appear as a gravitational weight. For each projectile mass, $|\mathbf{F}_P|/g$ reaches a global maximum after

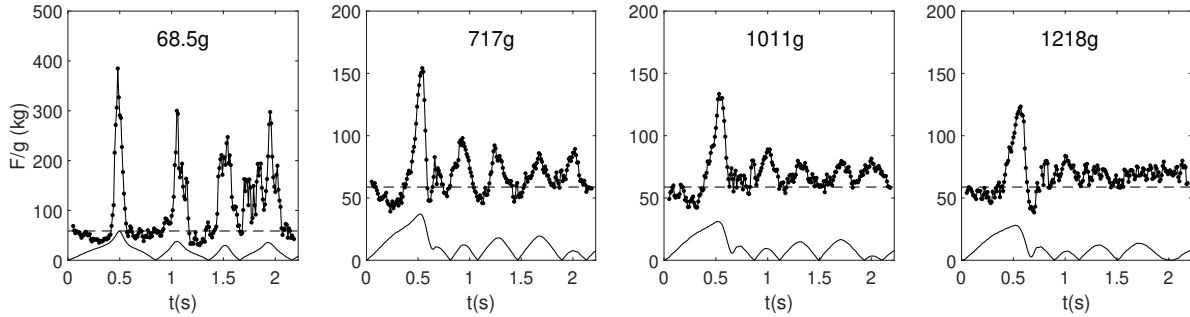


Figure 17. Full points: Reaction force $|\mathbf{F}_P|$ at pivot in units of mass for four projectile masses. Broken line: Final value $M + m_b$. Full curve: $|\dot{\theta}|$ in arbitrary units.

about 0.5s when the initial fall of the counterweight is stopped, and the angular speed $|\dot{\theta}|$ also has a maximum here. The maximum of $|\mathbf{F}_P|/g$ is quite high with the light projectile for which it almost reaches 400kg, and the secondary maxima that follow go as high as 300kg. With the heavier projectiles, the global maxima are more than a factor of two smaller and the secondary maxima are progressively reduced such that they have almost

disappeared at $m = 1218\text{g}$, where \mathbf{F}_P/g is close to the final value of $M + m_b = 58.76\text{kg}$ already after one second. The maxima of the angular speeds $|\dot{\theta}|$ almost coincide with the maxima of $|\mathbf{F}_P|/g$.

The accumulated loss of mechanical energy due to friction at time t is

$$Q_f = \int_0^t P_f(t') dt',$$

with P_f from (8), and the aerodynamic loss from the sling motion is

$$Q_a = \frac{1}{2} C \rho_d A_P \int_0^t v_m^3(t') dt',$$

where (B.2) is used. The two terms in the frictional loss Q_f and the aerodynamic contribution Q_a are shown separately in the upper panel of figure 18. The loss at

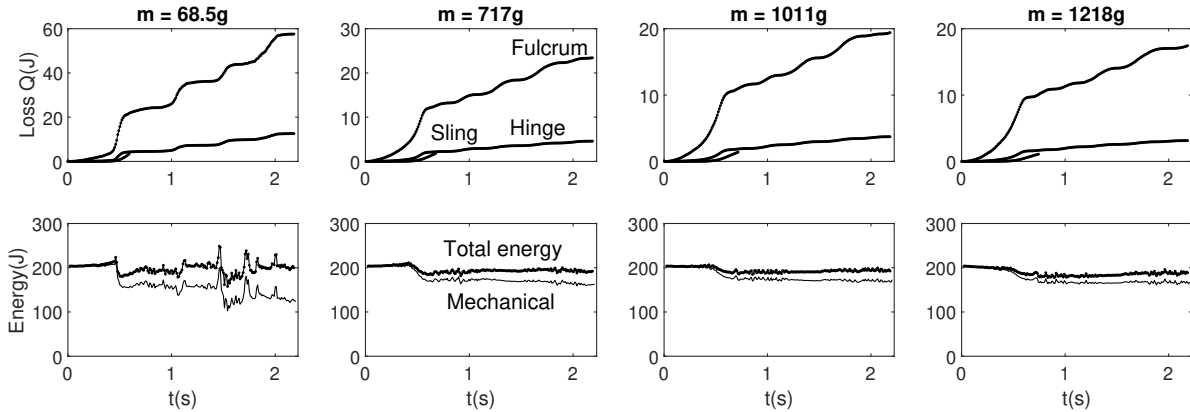


Figure 18. Upper panel: Frictional losses at fulcrum for beam and hinge for counterweight. Aerodynamic loss for sling. Friction coefficients: $\mu_f = \mu_h = 0.35$. Radii: $R_P = 1.7\text{cm}$ and $R_H = 0.25\text{cm}$. Aerodynamic constant $C = 0.25$, $\rho_d = 1.225\text{kg/m}^3$ and $A_P = 0.01\text{m}^2$, see Appendix B.2. Lower panel: Total mechanical energy as in figure 16 and total energy including losses.

the fulcrum dominates the frictional losses because the sliding speed is larger $R_P\dot{\theta} \gg R_H(\dot{\theta} - \dot{\psi})$ and the reaction forces are almost equal. The aerodynamic component is first quite small, but finally rises to approach the loss at the hinge.

The lower panel in figure 18 shows the sum of total mechanical energies and calculated losses. Energy is conserved, so this sum should equal the initial energy ΔU at all times. The sum is seen to be a little low, but the deviations for the heavier projectiles are quite small and possibly due to missing degrees of freedom as discussed earlier.

3.6. Semi-empirical ranges. Ballistics in air

The experimental data discussed so far were obtained in a laboratory with sufficient distances to ceiling and walls to safely accommodate sling and projectile throughout an entire shot. The projectiles reached maximum heights $\simeq 3\text{m}$, and were shot into and captured by a tightly packed pile of straw just in front of the trebuchet. The vacuum

ranges, R_v , derived from the measurements were corrected for aerodynamic losses along the ballistic path to give semi-empirical calculated ranges in air, R_a . The expressions used for vacuum ranges and losses are given in Appendix B.1 and Appendix B.2.

3.7. Field measurements of range

To test these semi-empirical ranges, the trebuchet was taken out to a flat field on warm days with little wind (close to standard temperature and pressure) and fired with two projectile masses m and two lengths of the sling L_4 . Many shots with different settings of the spigot were required in each case to find the longest field range R_f , and this effort required the work of at least two people. One to load and fire the trebuchet, and another to observe and log where the projectile hits ground. The spigot has markings for easy and reproducible setting, and is shown in figure 19. The force that act on it with a heavy projectile rises briefly to $\simeq 250N$. This necessitates hardening after machining to prevent bending.

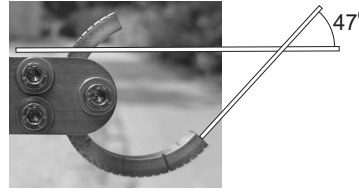


Figure 19. Semicircular spigot clamped to beam by three bolts. Spigot angle shown.

Semi-empirical predictions from the present experiments, field measurements and purely theoretical values are listed in table 3. The random errors of the semi-empirical values R_v are calculated from identical, repeated shots, and the larger uncertainty for R_a comes from an empirical, aerodynamic constant C , see Appendix B.2. The random

| | L_4 m | m g | R_v m | R_a m | α_v | R_f m | α_f |
|----------------------------|------------|----------|----------------|----------------|------------|----------------|------------|
| Semi-empirical predictions | 0.87 | 717 | 37.5 ± 0.1 | 35.1 ± 0.5 | 50.0^0 | | |
| | 0.87 | 1011 | 29.0 ± 0.2 | 27.7 ± 0.5 | 58.5^0 | | |
| Field measurements | 0.87 | 700 | | | | 34.4 ± 1.5 | 36.2^0 |
| | 0.87 | 1011 | | | | 24.9 ± 1.5 | 32.5^0 |
| | 0.93 | 700 | | | | 37.5 ± 1.5 | 19.7^0 |
| Theoretical values | 0.87 | 717 | 42.8 | 39.5 | | | |
| | 0.87 | 1011 | 32.2 | 30.6 | | | |

Table 3. Semi-empirical maximum ranges in vacuum R_v and in air R_a . Ranges measured in the field R_f . Ab initio theoretical values of R_v and R_a . Predicted spigot angles α_v and field values α_f . Stones of mass density $\rho_p = 3\text{g}/\text{cm}^3$ and $C = 0.5$. The design parameters are those listed in table 1 except for the sling length L_4 of 0.93m used in the field.

errors for the field measurements R_f are based on several repetitions under the same experimental conditions as far as possible.

The field values R_f are seen to agree well within uncertainties with the semi-empirical predictions R_a (when disregarding a small difference of 17g in projectile mass, see figure 10a). The field data with the increased sling length of 0.93m also shows a longer range. This is in good agreement with the data in figure 14, which indicates a best sling length close to one meter.

The theoretical ranges in table 3 were found by the use of an internet facility [12] and by independent integrations. The ranges in air are several ($\simeq 4$) standard deviations longer than the field values. The calculations, however, disregard internal friction and aerodynamic losses during the acceleration of the projectile prior to its release. Figure 18 indicates a loss of mechanical energy at release for longest range of $\simeq 5\%$ and this loss is carried mostly by the projectile. Range and kinetic energy at release are approximately proportional, so $\Delta R/R \simeq \Delta T/T \simeq 5\%$. This estimate suggests that the inclusion of losses will lower the discrepancy significantly.

The predicted spigot settings α_v in table 3 are much larger than the ones used in the field α_f . We have assumed that the ring slides off the semicircular spigot immediately when the sling direction becomes perpendicular to the direction of the spigot. This seems to be a reasonable assumption because the ring glides easily on the spigot and is therefore close to the edge at the critical time. Ring, cord and pouch, however, all have some inertia so it takes a little extra time for the projectile to free itself from the pouch. This time is estimated by $\Delta t = \Delta\phi/\dot{\phi}$, where $\Delta\phi \simeq 1/3\text{rad}$ is taken from the differences of spigot angles in table 3 and $\dot{\phi} \simeq 15\text{rad/s}$ from figure 11d (spigot almost at rest, so $v \simeq L_4\dot{\phi}$). We find $\Delta t \simeq 20\text{ms}$ which is short indeed and a likely explanation for the discrepancy, but difficult to qualify further.

4. Optimized design

The experimental trebuchet was built on intuition and a desire to have a durable and safe engine. Theoretical optimization of lengths and masses was not attempted, but the sling length and projectile mass that gives the best product of range and kinetic energy at target was found experimentally for constant values of remaining parameters. The result is shown in the first row of table 4. The efficiency $\epsilon = 73\%$ is the estimated ideal

| R m | T J | L_1 cm | L_2 cm | L_3 cm | L_4 cm | D cm | H cm | M kg | m g | m_b kg | ϵ % | S_P % | u_P mm | u_{CM} mm |
|----------|----------|-------------|-------------|-------------|-------------|-----------|-----------|-----------|----------|-------------|-----------------|------------|-------------|----------------|
| 36.6 | 141 | 97.5 | 25.0 | 51.5 | 87.0 | 7.5 | 83.1 | 53.9 | 717 | 4.86 | 73 | 0.03 | 0.6 | 0.8 |
| 36.6 | 141 | 128 | 36.2 | 63.9 | 111 | 4.9 | 109 | 26.3 | 697 | 2.16 | 91 | 0.07 | 4.3 | 5.9 |
| 50 | 25 | 97.2 | 21.3 | 55.0 | 88.0 | 2.8 | 82.9 | 7.88 | 95 | 0.50 | 93 | 0.07 | 3.2 | 5.0 |
| 50 | 350 | 157 | 42.7 | 80.4 | 137 | 6.4 | 134 | 55.4 | 1281 | 4.51 | 91 | 0.08 | 5.2 | 7.4 |

Table 4. The experimental trebuchet and optimized design. Strain at pivot S . Deformation at pivot u_P and at center of mass u_{CM} .

value for the engine without losses. It is derived from the measured efficiency of $\simeq 70\%$ (see table 2) and engine losses of $\simeq 5\%$.

The three remaining rows of table 4 show optimized design obtained as described in [7]. However, the analytical procedures laid out there do not cover small designs like the present, so ab initio numerical calculations were done in each case. The first has the same capacity as the experimental trebuchet, but it is $\simeq 25\%$ larger, the counterweight and the beam are $\simeq 50\%$ lighter, and the ideal engine efficiency has risen to 91%. The remaining two optimized design have a longer range of $R = 50\text{m}$ and different kinetic energies at target T . The one with $T = 25\text{J}$ has the same height H of the fulcrum as the experimental design and throws the projectile a distance of 60 times the height, but the projectile is light. The other with $T = 350\text{J}$ has about the same counterweight mass as the experimental design and throws a much heavier projectile, but the distance relative to height is reduced to 37. The optimized design have significantly improved efficiencies, and are generally much lighter and slightly larger.

The small beam masses m_b and diameters D bring up the question of strength so we show explicitly in table 4 values of strain S and deformation u . When the trebuchet is loaded prior to a shot, soldiers pull the beam down with ropes attached near the spigot. The bending is largest when the beam is horizontal and the quasi-static reaction force at the fulcrum from the trestle is then $F_s = Mg(1 + L_2/L_1)$. The strain varies along the beam and is largest at the fulcrum where the curvature $\partial^2u/\partial x^2$ is at its maximum. Strain and curvature are related by

$$S = \frac{D}{2} \frac{\partial^2 u}{\partial x^2}, \quad \text{and at the pivot} \quad \mathcal{M}_e \mathcal{I} \frac{\partial^2 u}{\partial x^2} \Big|_P = F_s \frac{L_1 L_2}{L_1 + L_2}$$

where \mathcal{M}_e is Young's modulus and $\mathcal{I} = (\pi/64)D^4$ the second moment of area. The deformations relative to a rigid beam at the pivot and at the center of mass or middle of the beam are, respectively,

$$u_P = \frac{1}{3} \frac{F_s}{\mathcal{M}_e \mathcal{I}} \frac{L_1^2 L_2^2}{L_1 + L_2} \quad \text{and} \quad u_{CM} = \frac{1}{16} \frac{F_s}{\mathcal{M}_e \mathcal{I}} L_2 (L_1 + L_2)^2.$$

The static values given in table 4 are small and considered safe with $S_P \ll 1\%$. The maximum deformation is found close to the center of mass and here it is only a few millimeters per meter of beam length, and much smaller with the experimental design. The load on the beam varies during a shot and may rise briefly to a few times Mg , but the strengths remain sufficient.

5. Summary and conclusions

A wealth of information can be extracted from a measurement of the inner movement of a trebuchet during only a single shot. It is therefore affordable in terms of time to carry out systematic studies of dependencies on several parameters. Maximum projectile range is a key variable, so it was emphasized and measured as a function of projectile mass, length of sling, and counterweight mass. Loss of range by friction and aerodynamics was estimated, and predicted ranges were compared with measured field ranges. The kinetic and potential energies of the projectile at release are important too and were also

derived. The sum is the vacuum value of the mechanical energy delivered to a target at the level of the engine.

The measured total mechanical energy must be a decreasing function of time because of inevitable irreversible losses. If it rises even briefly, a degree of freedom that absorbs and releases energy is overlooked or a constant like the moment of inertia for the beam is determined incorrectly. The total mechanical energy is thus a diagnostic tool and was used as such to exclude some measurements concerning the inner movement of the engine long after release for small projectile masses.

Loss of mechanical energy during acceleration of the projectile by the engine is mainly due to friction at bearings and hinges, but aerodynamic drag on the sling also contributes. All losses were determined, and when added to the derived mechanical energies, the resulting total energy was found to be approximately constant provided the projectile mass was not too small. The losses then amount to $\simeq 5\%$ of the available mechanical energy of $\simeq 200\text{J}$, and the efficiency at longest range is near 70% for a projectile mass $\simeq 700\text{g}$. The ideal engine efficiency in the absence of losses is $\simeq 73\%$, but an optimized design with the same capacity has $\epsilon = 91\%$.

The acceleration of the projectile at release projected on its velocity is almost zero at 700g, but positive for smaller masses and negative for larger. The kinetic energy T of lighter projectiles is thus still increasing at release, so delaying this a little to maximize the merit function $\mathcal{M} = RT$ increases the kinetic energy at target T , but reduces R . For heavier projectiles where the acceleration is negative at release so that the projectile works back on the engine, an earlier release has the same effect.

The reaction force at the fulcrum rises briefly during a shot to values near three times the gravity Mg of the counterweight or even more for light projectiles. The horizontal component approaches Mg . These forces determine friction losses and required strengths of beam, axles, bearings, and trestle. The size of the sling force on the projectile increases briefly to $\simeq 25mg$. Ropes, pouch, and spigot must be strong enough to withstand this load.

APPENDIX

Appendix A. Beam with fittings and model for moment of inertia

The weights of the fittings that hold spigot and counterweight are represented in a simple model for the beam by two point masses \tilde{m}_1 and \tilde{m}_2 placed at the respective distances \tilde{L}_1 and \tilde{L}_2 from the pivot. These four parameters are related to measured parameters by

$$\begin{aligned} m_b &= \hat{m} + \tilde{m}_1 + \tilde{m}_2 \\ m_b L_{CM} &= \frac{1}{2} \hat{m} (L_1 - L_2) + \tilde{m}_1 \tilde{L}_1 - \tilde{m}_2 \tilde{L}_2 \\ \mathcal{I}_b &= \frac{1}{3} \hat{m} (L_2^2 - L_1 L_2 + L_1^2) + \tilde{m}_1 \tilde{L}_1^2 + \tilde{m}_2 \tilde{L}_2^2, \end{aligned}$$

where \hat{m} is the beam mass without fittings, and remaining parameters are given in table 1. The four model parameters are collected on the left hand side of the matrix equation

$$\begin{Bmatrix} 1 & 1 \\ \tilde{L}_1 & -\tilde{L}_2 \\ \tilde{L}_1^2 & \tilde{L}_2^2 \end{Bmatrix} \begin{Bmatrix} \tilde{m}_1 \\ \tilde{m}_2 \end{Bmatrix} = \begin{Bmatrix} m_b - \hat{m} \\ m_b L_{CM} - \frac{1}{2} \hat{m} (L_1 - L_2) \\ \mathcal{I}_b - \frac{1}{3} \hat{m} (L_2^2 - L_1 L_2 + L_1^2) \end{Bmatrix} \quad (A.1)$$

and measured parameters on the right hand side. Equation (A.1) written as $\mathbf{A}\tilde{\mathbf{m}} = \mathbf{B}$ has the least squares solution $\tilde{\mathbf{m}} = (\mathbf{A}^T \mathbf{A})^{-1} \mathbf{A}^T \mathbf{B}$ and the distance D from this to a common solution is $D = D(\tilde{L}_1, \tilde{L}_2, \mathcal{I}_b) = (\mathbf{A}\tilde{\mathbf{m}} - \mathbf{B})^T(\mathbf{A}\tilde{\mathbf{m}} - \mathbf{B})$. Therefore, for any choice of two of the three parameters $(\tilde{L}_1, \tilde{L}_2, \mathcal{I}_b)$ the third is determined by $D = 0$ and a common solution for $\tilde{\mathbf{m}}$ is then found by solving the normal equations (A.1). Table A1 shows such common solutions, $\tilde{\mathbf{m}} = \{\tilde{m}_1, \tilde{m}_2\}^T$, for three values of \mathcal{I}_b , that cover the

| \tilde{L}_2 cm | $L_2 - \tilde{L}_2$ cm | $\mathcal{I}_b = 1.70 \text{kgm}^2$ | | | $\mathcal{I}_b = 1.85 \text{kgm}^2$ | | | $\mathcal{I}_b = 2.00 \text{kgm}^2$ | | |
|---------------------|---------------------------|-------------------------------------|---------------------|---------------------|-------------------------------------|---------------------|---------------------|-------------------------------------|---------------------|---------------------|
| | | $L_1 - \tilde{L}_1$ cm | \tilde{m}_1 kg | \tilde{m}_2 kg | $L_1 - \tilde{L}_1$ cm | \tilde{m}_1 kg | \tilde{m}_2 kg | $L_1 - \tilde{L}_1$ cm | \tilde{m}_1 kg | \tilde{m}_2 kg |
| 20 | 5 | 19.2 | 1.63 | 0.02 | 9.8 | 1.48 | 0.17 | 0.4 | 1.37 | 0.28 |
| 25 | 0 | 19.2 | 1.63 | 0.02 | 10.3 | 1.50 | 0.15 | 1.4 | 1.39 | 0.26 |

Table A1. Model parameters that satisfy (A.1).

experimental uncertainty in table 1, and two choices of \tilde{L}_2 . When $\mathcal{I}_b = 1.85 \text{kgm}^2$, most of the mass $\tilde{m}_1 + \tilde{m}_2 = 1.65 \text{kg}$ is placed at a reasonable distance of $L_1 - \tilde{L}_1 \simeq 10 \text{cm}$ from the long end of the beam irrespective of \tilde{L}_2 . For the two other values of \mathcal{I}_b , this distance is either too long ($\simeq 20 \text{cm}$) or too short ($\simeq 1 \text{cm}$). This result consolidates the value and uncertainty of \mathcal{I}_b in table 1.

Appendix B. Range

Appendix B.1. Range in vacuum

The vacuum range R_v measured from the horizontal position of the fulcrum to impact on ground at the level of the trough is

$$R_v = \frac{v_i^2}{2g} \left(\sin(2A) + \sqrt{\sin^2(2A) + \frac{8gy_i}{v_i^2} \cos^2(A)} \right) - x_i. \quad (\text{B.1})$$

Here \mathbf{v}_i is the initial velocity at release and $v_i = |\mathbf{v}_i|$ the speed, (x_i, y_i) the horizontal position and height, and A the angle of \mathbf{v}_i relative to the horizontal plane. The parameters x_i and y_i are given by (5) in terms of θ and ϕ , and \mathbf{v}_i and A follow by differentiation:

$$\begin{aligned} \mathbf{v}_i &= (L_1 \cos \theta \dot{\theta} + L_4 \sin \phi \dot{\phi}) \mathbf{e}_x + (L_1 \sin \theta \dot{\theta} - L_4 \cos \phi \dot{\phi}) \mathbf{e}_y \\ A &= \arctan \left(-\frac{v_{iy}}{v_{ix}} \right) \quad \text{with} \quad v_{ix} < 0. \end{aligned}$$

Appendix B.2. Range in air

The aerodynamic force is modeled by

$$\mathbf{F}_a = -\frac{1}{2} C \rho_a A_P v^2 \mathbf{e}_v. \quad (\text{B.2})$$

Here $C \simeq 1/2$ is an empirical constant that depends on the shape and roughness of the projectile with aerodynamic cross section A_P and speed v . The air density is ρ_a and \mathbf{e}_v is a unit vector along the path.

We assume that the aerodynamic loss is much smaller than the mechanical energy of the projectile and that the vacuum range is much larger than the size of the engine. The loss Q can then be estimated by perturbation theory applied to a symmetric ballistic vacuum trajectory without losses that starts at $(-R_v/2, 0)$ and ends at $(R_v/2, 0)$

$$Q = \int_{-T/2}^{T/2} (\mathbf{F}_a \cdot v \mathbf{e}_v) dt = C \rho_a A_P \int_0^{T/2} v^3 dt,$$

where

$$\frac{T}{2} = \frac{v_i \sin(A)}{g} \quad \text{and} \quad v^2 = (v_i \cos(A))^2 + (gt)^2.$$

With the substitution $t = (v_i \cos A / g) \tau$ one finds

$$Q = C \rho_a A_P \frac{v_i^4}{g} \cos^4(A) \int_0^{\tan(A)} (1 + \tau^2)^{3/2} d\tau, \quad (\text{B.3})$$

and the relative loss is

$$\frac{Q}{E} = 4\pi \left(\frac{4\pi}{3} \right)^{-2/3} \frac{C \rho_a}{g \rho_s^{2/3}} \frac{E}{m^{4/3}} \frac{\mathcal{F}}{(\tan^2(A) + 1)^2}, \quad (\text{B.4})$$

where \mathcal{F} is the definite integral in (B.3). We have also used $E = (1/2)mv_i^2$, $A_P = \pi r_p^2$ and $m = \rho_s(4\pi/3)r_p^3$, where ρ_s is the density of stone. The function \mathcal{F} was evaluated analytically, and with $x = \tan(A)$ the angular dependence in (B.4) is

$$\frac{\mathcal{F}(x)}{(x^2 + 1)^2} = \frac{3 \sinh^{-1}(x) + x(2x^2 + 5)\sqrt{x^2 + 1}}{8(x^2 + 1)^2}.$$

This is almost constant in the interval from 30° to 50° and is replaced by the value at $A = 40^\circ$. With $\rho_a = 1.225\text{kg/m}^3$, $\rho_s = 2700\text{kg/m}^3$ and $C = 0.5$ we find in SI units

$$\frac{Q}{E} = 6.2 \cdot 10^{-4} \frac{E}{m^{4/3}} = 3 \cdot 10^{-3} \frac{R}{m^{1/3}}. \quad (\text{B.5})$$

The continuing loss of mechanical energy along the path shortens the range such that approximately

$$\frac{\Delta R}{R} = \frac{1}{2} \frac{Q}{E}, \quad (\text{B.6})$$

which is the vacuum range calculated with the reduced initial velocity $(v_i + v_f)/2$, where $mv_f^2 = 2(E - Q)$. The expressions (B.5) and (B.6) hold when Q is somewhat less than E and slightly overestimate the reductions because they are calculated with a trajectory that is too long and the velocities along the trajectory are also too large.

References

- [1] Hansen, P. V., *Acta Archaeologica*, **63**, (1992), pp189-268
- [2] Chevedden, P. E. (2000), *Dumbarton Oaks Papers*, 54. Washington D.C.
- [3] Saimre T., *Estonian Journal of Archaeology*, (2006), **10**, 1, pp61-80
- [4] Chevedden, P. E., Eigenbrod, L., Foley, V., and Soedel, W. (1995), *Sci. Am.* **273**, pp66-71.
- [5] Fulton M. S., Chrassis N. G., Phillips J. and Kedar B. Z. *Crusades*, (2017), **16**, pp33-53
- [6] Fulton M. S., *Artillery in the Era of the Crusades: Siege Warfare and the Development of Trebuchet Technology*. *History of Warfare*, vol. 122, BRILL (2018)
- [7] Horsdal E., arXiv e-prints, arXiv:2303.01306
- [8] O'Connell J., *The Physics Teacher* 39, 471 (2001); <https://doi.org/10.1119/1.1424595>
- [9] Denny M., *Eur. J. Phys.* 26 561 (2005)
- [10] Denny M., *The Physics Teacher* 47, 574 (2009); <https://doi.org/10.1119/1.3264587>
- [11] Christo Z., *Phys. Educ.* 52 013010 (2017)
- [12] <https://virtualtrebuchet.com/simulator>